RESEARCH ARTICLE

ADVANCED OPTICAL MATERIALS
www.advopticalmat.de

Tailoring Chiral Gold Nanorods via Single-Step Seed-to-Au(III) Ratio and Unlocking their Potential in Refractive Index Sensing

*Carlos Fernández-Lodeiro, Sergio Gómez-Grana, María José Cordero-Ferradás, Victor F. Martín, Wiebke Albrecht, Pablo Hervés, Lakshminarayana Polavarapu, José M. Taboada, Fernando Obelleiro, Sara Bals, Jorge Pérez-Juste, and Isabel Pastoriza-Santos**

Dedicated to Prof. Luis Liz-Marzán on the occasion of his 60th birthday

Colloidal chiral plasmonic nanoparticles are garnering growing interest due to their interaction with circularly polarized light, offering advanced optical applications. Their circular dichroism (CD) spectra are significantly narrower and more defined than extinction spectra, making them ideal for refractive index-based sensing. Despite progress in colloidal synthesis, this field remains relatively underexplored. In this work, a one-step, seed-mediated route to chiral Au nanorods is introduced in which the molar ratio Au^{3+}/Au^{0} enables continuous control of the CD response (intensity, sign, and position), using *L*- and *D-cysteine* as chiral inducers. CD-based refractive index sensitivity (RIS) measurements reveal a figure of merit (FoM = RIS/linewidth) exceeding 1000 RIU^{-1}, outperforming the conventional extinction-based approaches. Thin films of C-AuNRs fabricated via a layer-by-layer assembly retain the bisignate CD response and show RIS values comparable to colloidal samples. These films demonstrate excellent stability, reusability, and resilience in highly absorbing media. All the experimental data are supported by advanced calculations performed using full-wave M3 Maxwell's solver and using electron tomography reconstructions as direct input. Finally, their applicability in RI-based quantitative detection of bovine serum albumin (BSA) is demonstrated, highlighting their potential for biomolecular sensing.

1. Introduction

The unique interaction of light with nanoscale materials has led to groundbreaking advancements in the field of nanoscience and nanotechnology. Among the diverse array of nanoscale phenomena, chirality, a property traditionally associated with molecular structures, has emerged as a key phenomenon for many important optical applications.[1,2] Chiral nanostructures, composed of metals,[3] semiconductors,[4] or dielectric materials,[5] exhibit unique interactions with circularly polarized (CP) light, leading to distinctive optical effects such as circular dichroism, CP luminescence, and optical activity.[6–10] These properties render chiral nanoparticles (NPs) promising for applications in optics,[11] catalysis, and, most notably,[12] sensing.[13] In this context, the field of chiral plasmonic nanoparticles has advanced significantly over the past few years.[6]

C. Fernández-Lodeiro, S. Gómez-Grana, M. J. Cordero-Ferradás, P. Hervés, L. Polavarapu, J. Pérez-Juste, I. Pastoriza-Santos
CINBIO
University of Vigo
Vigo 36310, Spain
E-mail: pastoriza@uvigo.es

The ORCID identification number(s) for the author(s) of this article can be found under https://doi.org/10.1002/adom.202502575

DOI: 10.1002/adom.202502575

V. F. Martín
Departamento de Teoría de la Señal y Comunicaciones y Sistemas Telemáticos y Computación
Universidad Rey Juan Carlos
Fuenlabrada 28942, Spain

J. M. Taboada
Departamento de Tecnología de los Computadores y de las Comunicaciones
University of Extremadura
Cáceres 10003, Spain

F. Obelleiro, S. Bals
Departamento de Teoría de la Señal y Comunicaciones
University of Vigo
Vigo 36310, Spain

The continuous global research efforts on plasmonic NPs have enabled the development of advanced synthesis strategies for precise control over nanoparticle morphology, optical properties, and functionalization.[6,14–16] Currently, these strategies are being extended to chiral plasmonic NPs through chiral molecular-induced growth and systematic variation of synthesis parameters to enhance their dissymmetry factors (g-factors).[17] The g-factor, a dimensionless parameter that helps eliminate concentration dependence,[18] quantifies the efficiency of the chirooptical response.[19] Among the variety of chiral nanostructures reported in the literature, colloidal chiral gold nanorods (C-AuNRs) and helicoids prepared by seeded growth have garnered significant attention due to their unique optical properties and tunable chiroptical activity.[7,20–23] These are typically synthesized through multi-step chiral seeded growth, where chiral nanoparticles from each preceding step serve as seeds for the next, enabling precise tuning of their chiroptical response.[3] These nanostructures have begun to attract significant attention for biosensing applications.[24] However, to date, most studies primarily focus on analyte-induced circular dichroism (CD) responses, enabling quantitative biosensing. One of the most promising plasmonic sensing approaches involves detecting changes in the local refractive index (RI) produced by the presence of an analyte through variations in the localized surface plasmon resonance (LSPR) of a plasmonic nanostructure.[6,25] This sensing technology has played a crucial role across various scientific fields, including physics, chemistry, biology, and medicine.[26] The ability to detect minute variations in RI is crucial for a wide range of applications, including environmental monitoring,[27] biomedical diagnostics,[28] and molecular sensing.[29,30] While extensive research has been conducted using achiral plasmonic NPs for RI-based sensing,[31] the application of chiral colloidal NPs in this context remains less explored. Considering the narrower CD response compared to the broad extinction bands, chiral nanostructures offer a promising alternative for RI-based sensing. Indeed, several studies have demonstrated that CD-based sensing outperforms conventional extinction-based methods, offering superior resolution and sensitivity.[30] A key feature is that the circular polarization-dependent extinction of the chiral NPs is characterized by rich spectral features, including bipolar peaks and nulls, suitable for tracking refractive index changes. This sensing modality offers strong optical contrast even in the presence of highly absorbing media, an important consideration for use in complex biological media with limited transmission. However, these approaches often rely on chiral nanostructures fabricated via physical vapor deposition techniques, which limits their scalability, flexibility in terms of use, and practical deployment.[30]

In contrast to multi-step seeded approaches commonly used to modulate the chiroptical response of AuNRs,[3] here we introduce a single-step method in which the molar ratio $R = [Au^{3+}]/[seed]$ serves as the unique tuning parameter. Starting from achiral seeds and adding L- or D-cysteine, varying R continuously adjusts the CD response (intensity, sign, and spectral position) without iterative overgrowth. The structural origin of the optical activity is validated by combining 3D electron tomography with full-wave simulations that use the reconstructed solid as direct input. This scheme not only streamlines and scales the synthesis, but it also enables, for the first time to our knowledge, CD-based refractive-index sensitivity (RIS) measurements of colloidal C-AuNRs and their thin-film counterparts. These chiral plasmonic substrates, having sensing capability with a high figure of merit (FoM), mark a significant advancement in plasmonic sensing technologies. Furthermore, aiming to demonstrate their practical applicability, the C-AuNR-based substrates were tested for RI-sensing in optically dense environments and the quantitative detection of bovine serum albumin (BSA).

2. Results and Discussion

C-AuNRs were synthesized by a single-step seed-mediated growth method, wherein achiral AuNR seeded were first grown at 40 °C through the reduction of $HAuCl_4$ by ascorbic acid (AA) in the presence of cetyltrimethylammonium chloride (CTAC) surfactant. The chiral growth and the handedness were controlled by the addition of chiral molecules, *L-cysteine* or *D-cysteine*, in the growth solution. This approach differs from the multi-step growth method of C-Au NRs, where the optical properties were tuned by the successive overgrowth of C-Au NRs obtained at each preceding step.[3] Here, we controlled the optical response of C-AuNRs in a facile single-step approach by controlling the ratio of achiral AuNRs to Au (III) ions in the growth solution, enabling rapid synthesis of C-AuNRs with desired optical response. The achiral AuNR seeds had an average length of 79 ± 6.7 nm and an average width of 32 ± 1.4 nm (Figure S1, Supporting Information), displaying longitudinal and transverse LSPR bands centered at 684 and 517 nm, respectively. To synthesize C-AuNRs, the $[Au^{3+}]$/[AuNR seeds] molar ratio (R) was set to 10, and the concentration of *L-* or *D-cysteine* was optimized to 0.13 nM. Note that [AuNR seeds] refer to the gold atom concentration in the seed solution, using the standard calibration introduced by Scarabelli et al.[32] Next, to tune both the optical and chiroptical properties of the C-AuNRs, R was systematically varied while keeping the Au salt concentration constant (**Figure 1A**, see experimental section for details). Figure 1B shows the vis–NIR spectra of the C-AuNRs obtained at R values ranging from 4 to 20. At lower R values (4–7), the particles still exhibit distinct longitudinal and transversal LSPRs, which progressively merge into a single broad band at higher R values (10–20). The chiroptical properties of C-AuNRs prepared with *L-cysteine* showed a bisignate CD response with a main negative peak that gradually redshifted from 557 to 612 nm as R increased (Figure 1C). The highest CD intensity was observed at $R = 10$. Interestingly, similar trends were observed with *D-cysteine*, but with opposite CD signals, while no CD was detected in the presence of racemic *cysteine* (Figure S2, Supporting Information). These results demonstrate that the chiroptical properties of the synthesized C-AuNRs could be finely tuned across a narrow visible range by simply controlling R.[3,33,34]

W. Albrecht
Electron Microscopy for Materials Research (EMAT) and NANOlab Center of Excellence
University of Antwerp
Antwerp 2020, Belgium
W. Albrecht
LMPV-Sustainable Energy Materials Department
AMOLF
Science Park 104, Amsterdam 1098 XG, The Netherlands

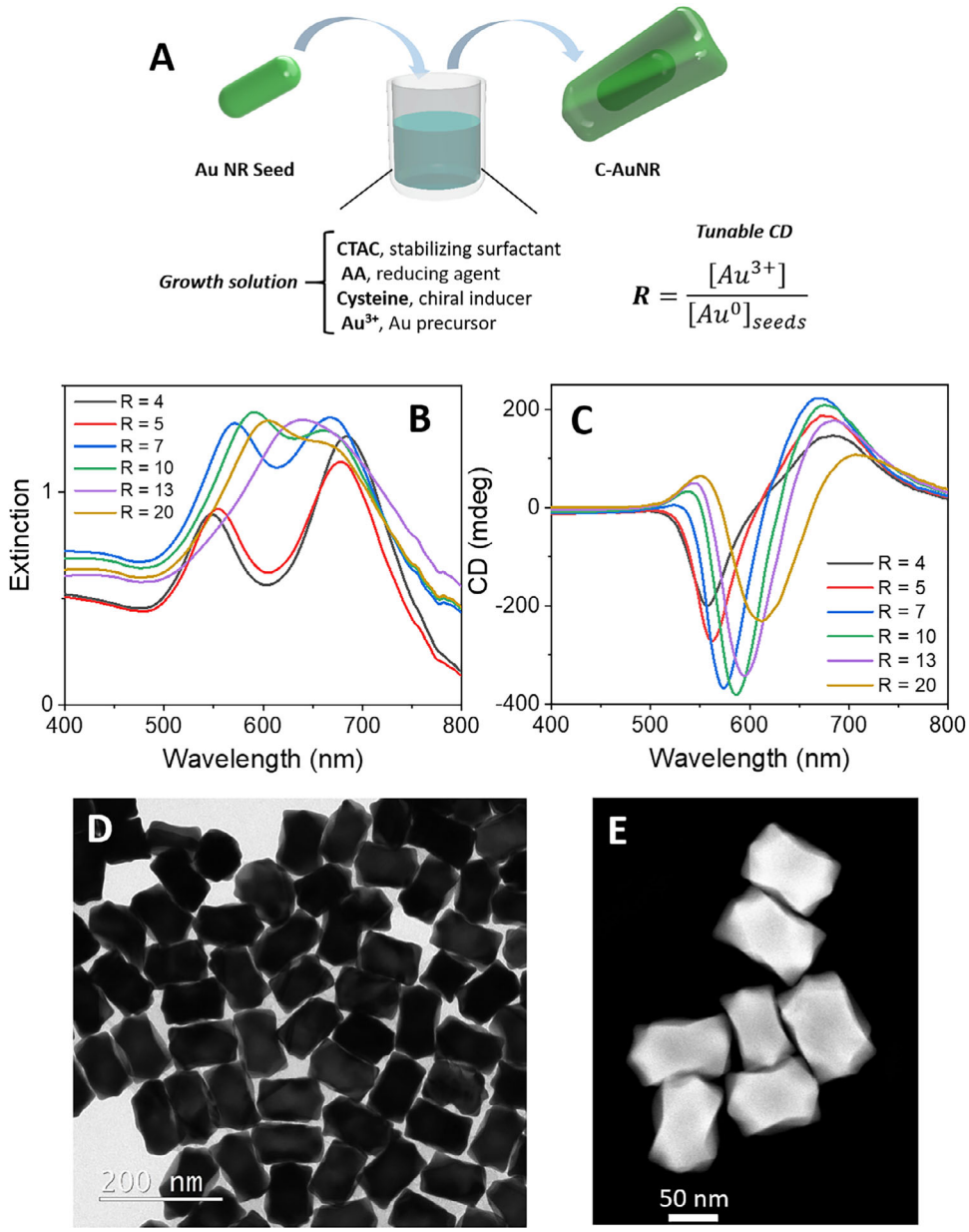

Figure 1. A) Schematic of the seed-mediated synthesis of C-AuNRs using *L*- or *D-cysteine*. B,C) Normalized extinction (B) and CD (C) spectra of C-AuNRs grown using various Au^{3+}/AuNR seed molar ratios, *R*, ranging from 4 to 20. D,E) Representative TEM (D) and STEM (E) images for C-AuNRs synthesized using *L-cysteine* with a $R = 10$.

The transmission electron microscopy (TEM) analysis (Figure 1D; Figure S3, Supporting Information) revealed that as *R* increased, the aspect ratio of C-AuNRs decreased from 2.5 for AuNR seeds to 1.3 for C-AuNRs synthesized at $R = 20$, in agreement with the observed evolution of their optical properties (Figure 1A). This behavior was mainly attributed to an increase in the width of AuNRs. Moreover, tip protrusions were observed on the C-AuNRs (Figure 1D,E; Figure S3, Supporting Information). Table S1 (Supporting Information) summarizes the average dimensions of the resulting C-AuNRs. To further investigate the relationship between the morphology and the optical and chiroptical response, electron tomography analysis was performed. **Figure** 2A,B shows the electron tomography reconstruction of a single C-AuNR synthesized with an *R* of 10. A full reconstruction visualization videos are included as Videos SV1 and SV2 (Supporting Information). The particle presents a square cross-section with the four concave lateral facets with tilted ridges in agreement with the fourfold twisted morphology previously reported for overgrown AuNRs in the presence of *cysteine*.[3] Subsequently, the 3D object retrieved from electron tomography reconstruction was directly used as the input morphology for the theoretical modeling. This modeling was based on the numerical solution of Maxwell's equations employing the M^3 solver, which implements a full-wave frequency-domain

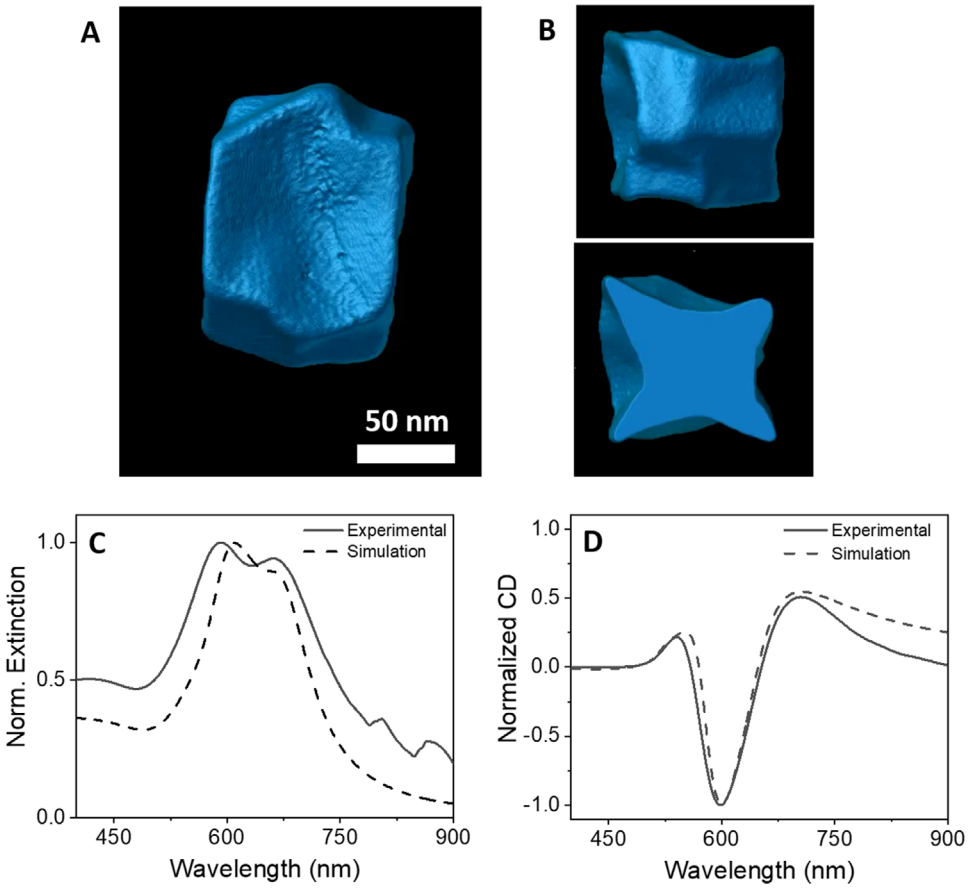

Figure 2. A,B) Snapshots from the electron tomography reconstruction of C-AuNR synthesized using *L-cysteine* at $R = 10$: lateral view (A) and tip view (B, top) and cross-sectional view (B, bottom). C,D) Experimental (solid line) and simulated (dashed line) optical properties of C-AuNRs: normalized extinction (C) and CD (D) spectra. [Correction added on October 31, 2025, after online publication: Figure 2 has been updated in this version]

methodology based on boundary-element parametrizations (see more details in the experimental part).[35] The resulting simulated optical and chiroptical properties clearly resemble those observed experimentally for the C-AuNR (Figure 2C,D), demonstrating that the twisted structure is responsible for the observed optical activity. It should be noted that for the morphology studied here, the simulated field enhancement distributions under opposite circular polarizations are almost complementary,[3] indicating that the strong plasmonic chiroptical activity arises primarily from the twisted structure along the nanorod length rather than from a single LSPR mode.

Considering the great potential of chiral nanostructures in RI-based sensing, we evaluated the sensing capabilities of our four-fold twisted C-AuNRs ($R = 10$, *L-cysteine*, Figure 2), studying the variation of the chiroptical properties induced by changes in their local RI when dispersing them in different water-glycerol mixtures.[30,36] We used the Lorentz-Lorenz model to calculate the RI of the mixtures.[37] **Figure** 3A shows the CD response of the *L*-C-AuNRs in different water-glycerol mixtures. The results indicated a redshift of the CD bands as the RI of the NP surrounding medium increased. Besides, it should be noted that the CD spectra are more feature-rich than the corresponding extinction spectra under unpolarized light (Figure S4, Supporting Information), and exhibit narrower bands.[30,38] Thus, in Figure 3A, we can identify two maxima (M1 at λ_{M1} and M2 at λ_{M2}), a minimum (m at λ_m), and two crossing points (1 at λ_1 and 2 at λ_1), which can be tracked in response to changes in the RI of the medium. Figure 2B presents the wavelength shifts ($\Delta\lambda$) of M1, M2, m, 1 and 2 versus RI, I, showing good linearity in all cases ($R^2 = 0.97$–0.99). The RI sensitivity (RIS), defined as the $\Delta\lambda$ per refractive index unit (RIU),[29] is estimated from the corresponding linear fit. The obtained RIS were 118.7, 157.8, 155.2, 282.9, and 470.4 nm/RIU for M1, 1, m, 2, and M2, respectively. Interestingly, the RIS depends on the selected chiroptical feature, and as expected, the highest sensitivities are achieved with the chiroptical features located at longer wavelengths (λ_2 and λ_{M2}). In conjunction with sensitivity, it is important to consider accuracy. Although sensitivity increases linearly with λ, the peak width also follows the same trend.[39] Notably, the spectroscopic resolution at zero-crossing can be estimated by performing a linear fit to the bipolar CD signal near the zero-crossing point (at λ_1 and λ_2), yielding a resolution ($\delta\lambda$) of 0.005 nm (Figure S5, Supporting Information).

Next, we calculated the FoM, defined as the ratio between the RIS and the full width at half-maximum (FWHM) at the corresponding CD feature. The FoM serves as a comprehensive metric to quantify the overall performance of a sensor and enables direct comparison with other sensing approaches.[39] It should be

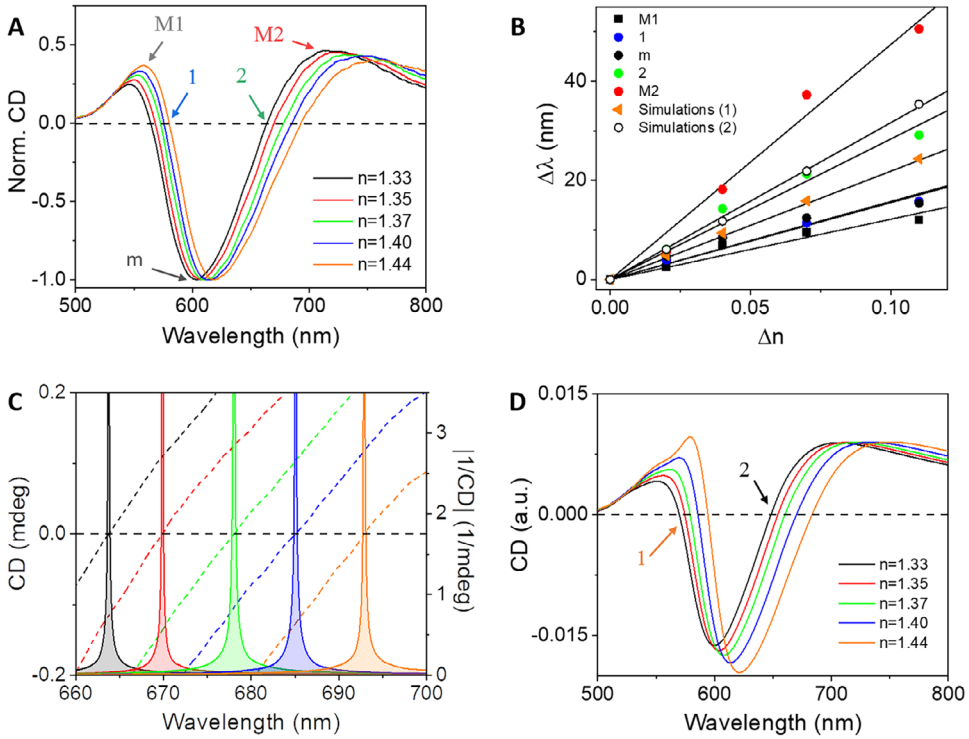

Figure 3. A) Experimental CD spectra of *L-cysteine* C-AuNRs ($R = 10$) dispersed in media with varying refractive indices, as indicated. B) Wavelength shifts ($\Delta\lambda$) of key spectral features relative to water ($n = 1.33$), along with simulated shifts at spectral feature 1 shown in D. The solid lines represent linear fits. C) CD (dashed lines) and inverse absolute CD ($|CD|^{-1}$, solid lines) at λ_1 for each refractive index medium. The color code is the same as in A. D) Simulated CD spectra of a single C-AuNR in media with different refractive indices. The arrows indicate the zero-crossing points (1) and (2), which were used to estimate the RIS value from the simulations.

noted that determining the FWHM of the M2 band remains challenging due to uncertainty regarding the endpoint of the band, and therefore, its FoM was not estimated. For the M1 and m bands, FWHM of 34.2 and 61.6 nm were measured, corresponding to FoM values of 3.5 and 2.5 RIU^{-1}, respectively. The zero-crossing points 1 and 2 were more precisely determined by plotting 1/|CD|, as shown in Figure 3C. These points are characterized by a diverging FoM, since 1/|CD| approaches infinity at the crossing. However, the FWHM can be estimated by accounting for experimental resolution in the determination of CD. Thus, assuming a resolution of 0.286 mdeg, the 1/|CD| spectra were truncated at 3.50 $mdeg^{-1}$ (Figure 3C),[40] resulting in FWHM values ranging from 0.18 to 0.37 nm. Considering an average FWHM of 0.28 nm, FoM values of 563.6 and 1010.4 RIU^{-1} were obtained (**Table 1**). These values greatly exceed those reported for plasmonic NPs synthesized by wet-chemical methods.[29,39,41]

To further validate these experimental observations, we simulated the CD spectra of our 3D model embedded in a medium with varying refractive indices ranging from 1.33 to 1.44. As shown in Figure 3D, a redshift in the main CD band is observed as the refractive index increases. Besides, the RIS at λ_1 and λ_2 were 217.2 and 316.9 nm/RIU, respectively, in good agreement with those obtained experimentally.

Next, we analyzed the sensing applicability of C-AuNRs ($R = 10$) immobilized on a glass substrate via a layer-by-layer strategy with polyelectrolytes (see Experimental Section for details). To

Table 1. Summary of the refractive index sensitivity (RIS) and figure of merit (FoM) estimated for the different CD and extinction spectral features of C-AuNRs ($R = 10$, *L-cysteine*).

Circular Dicroism			Extinction		
Spectral feature	RIS [nm/RIU]	FoM [RIU^{-1}]	Spectral feature	RIS [nm/RIU]	FoM [RIU^{-1}]
M1	118.7	3.5	λ_{max1}	123.0	1.9
1	157.8	563.6	λ_{max2}	249.9	2.1
M	155.2	2.5			
2	282.9	1010.4			
M2	470.5	n.d.			

n.d.: not determined.

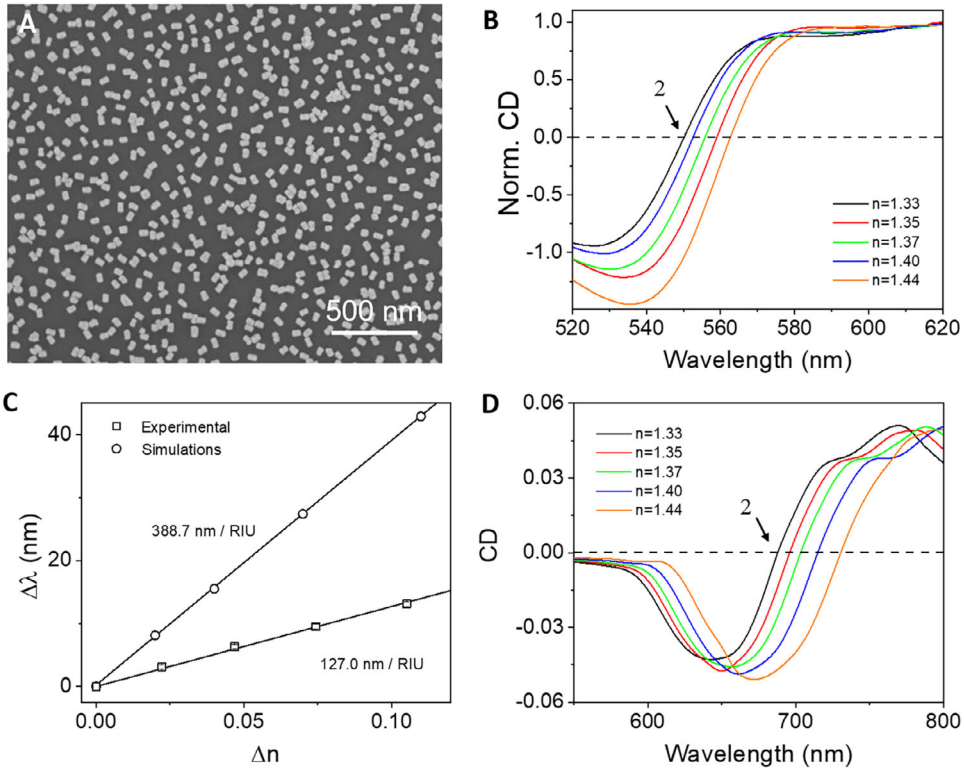

Figure 4. A) SEM image of C-AuNRs (R = 10, *L-cysteine*) deposited on a glass substrate forming a chiral thin film. The deposition time was 300 min. Scale bar in the inset: 100 nm. B) Experimental CD spectra of the chiral thin film embedded in media with different refractive indices, as indicated. C) Wavelength shift ($\Delta\lambda$) at the zero-crossing point (2) relative to water for simulated (circles) and experimental (squares) C-AuNR-based substrates. D) Simulated CD spectra of a substrate composed of a random distribution of 3000 C-AuNRs in different refractive index environments.

perform this study, we selected thin films obtained after 300 min deposition of C-AuNRs (for further details, see Figure S6 and discussion, Supporting Information). As shown in **Figure** 4A, C-AuNRs are uniformly distributed on the substrate with random orientation, forming a sub-monolayer (Figure 4A). The analysis of their chiroptical properties revealed a bisignate CD signal (Figure 4B), which confirmed its chiral nature. The RIS was subsequently evaluated by recording the CD spectra of the films in media with varying RIs (Figure 4B). A RIS value of 127.0 nm/RIU and a FoM of 453.6 were determined at the CD-zero-crossing point (2, Figure 4C). Interestingly, the sensitivity values of the chiral thin film closely match those of the colloidal dispersion (Figure 3B and Table 1). The reproducibility of the response was assessed by estimating the RIS of three independent plasmonic thin films under identical conditions (Figure S7, Supporting Information). In addition, the chiral thin film showed good recyclability as evidenced by the consistent RIS values maintained over multiple independent sensing cycles (Figure S8, Supporting Information). Furthermore, the RIS values obtained for chiral thin films with lower density coverages showed similar values (Figure S9, Supporting Information), indicating that the RIS is insensitive to coverage in our sub-monolayer regime. Similar results (RIS = 138.0 nm/RIU) were obtained for chiral thin films fabricated with C-AuNRs synthesized in the presence of *D-cysteine* (Figure S10, Supporting Information).

To gain a comprehensive understanding of the chiral thin films, we performed theoretical modeling, also employing the M^3 solver. The model used for the simulations consisted of a flat glass substrate with 3000 C-AuNRs randomly distributed on one side (Figure S11, Supporting Information), each NP identical and taken from the electron tomography reconstruction shown in Figure 2A. The simulated surface coverage was 17%, with an average interparticle distance of ≈3.25 nm. Considering the inherent complexity of developing a mechanistic colloidal deposition algorithm that accounts for the various attractive and repulsive forces required to produce a realistic CAD model of the deposition, we opted instead to construct a CAD model mimicking the SEM images in Figure 4A (see Figure S11, Supporting Information). Although all nanoparticles were modeled as identical, we reproduced their relative arrangement and orientation, and attempted to account for polydispersity effects by introducing certain variability in the interparticle distances (nonetheless, it should be noted that the statistical distribution of interparticle distances may not fully capture the experimental system, which could lead to spectral shifts). Simulations were conducted using the same RI values as those used in the experiments (n = 1.33–1.44). As shown in Figure 4D, the calculated CD spectra display the bisignate CD signal, which exhibited a redshift with increasing RI. RIS value, estimated at the zero-crossing CD wavelength (2, Figure 4D), obtained was 388.7 nm/RIU (Figure 4C). There is a discrepancy between the experimental and simulated RIS values (127.0 vs 388.7 nm/RIU), likely due to the idealized nature of the model, which assumes a perfectly monodisperse system of identical C-AuNRs. To investigate the relationship between

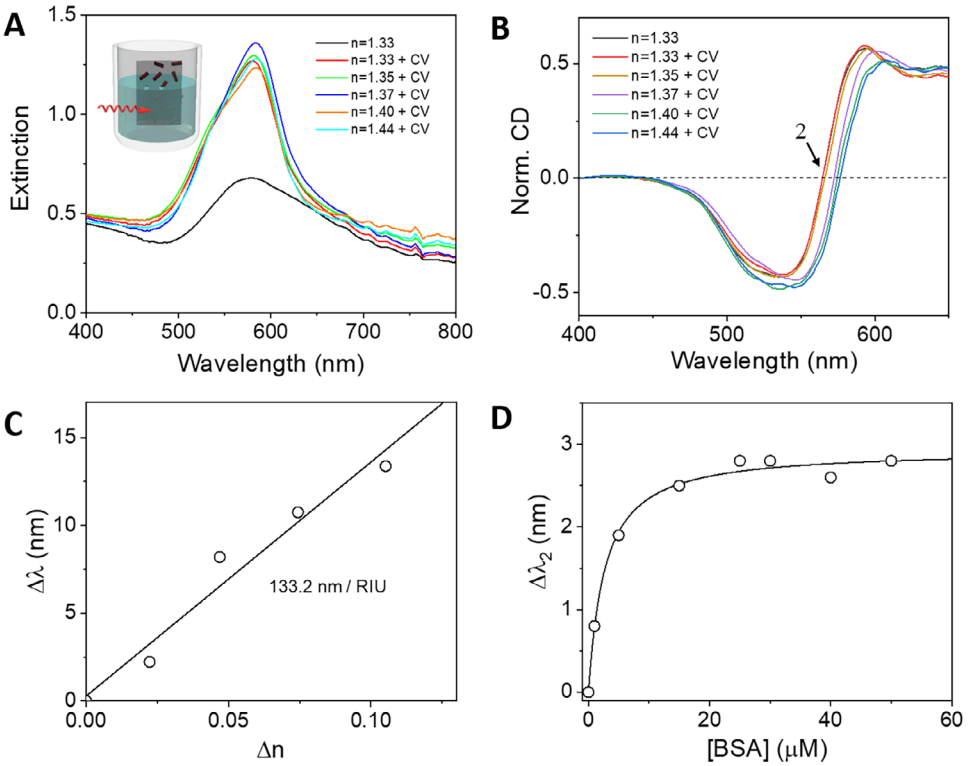

Figure 5. A,B) Extinction (A) and CD (B) spectra of a chiral thin film immersed in media with different refractive indices and containing 10 μM crystal violet (CV), as illustrated in the inset of (A). C) CD wavelength shift, relative to water (1.33), for the zero-crossing point (2), as shown in (B). D) CD zero-crossing point (2) change of the chiral thin film with the increase of aqueous concentration of BSA.

this discrepancy and the accurate modeling of the experimental statistical distribution, an additional set of simulations was carried out. Figure S12 (Supporting Information) illustrates the influence of single-particle orientation on the CD spectrum. Each curve corresponds to the CD response of a single nanoparticle as its orientation with respect to the excitation direction is varied through rotations around both the longitudinal and transversal axes, as depicted in Figure YYY. The results reveal a shift in the CD zero-crossing wavelength that depends on the particle orientation, with a more pronounced effect for transversal rotations. These orientation-dependent variations, combined with potential discrepancies arising from nanoparticle size and shape polydispersity as well as from the statistical distribution of interparticle distances, contribute to the spectral displacement observed in the simulations.

A key advantage in CD spectroscopy is its insensitivity to achiral absorbers or scatterers.[42,43] Therefore, unlike conventional extinction-based measurements, CD enables high signal-to-noise detection of chiral analytes even in strongly absorbing environments. To demonstrate this, we investigated the CD and extinction responses of a chiral thin film (Figure 4A) immersed in media of varying RI values and containing a strong molecular absorber (crystal violet, CV) in the LSPR region (**Figure 5**). While the extinction spectra (Figure 5A) become convoluted and show no clear spectral trend due to the presence of CV, the CD spectra (Figure 5B) remain largely unaffected, exhibiting multiple well-defined spectral features for RI-based sensing. Indeed, from the CD data analysis at the zero-crossing point (2 in Figure 5B), a RIS of 133.2 nm/RIU and FoM of 475.7 RIU^{-1} were obtained (Figure 5C). These values closely match those measured in the absence of CV (127.0 nm/RIU and a FoM of 453.6.1 RIU^{-1}), highlighting the robustness of CD-based sensing against background interference, particularly in optically complex media.

Finally, as proof of concept, we evaluated the potential of these chiral thin films for the RI-based detection of biologically relevant analytes.[44] We chose bovine serum albumin (BSA) as our model analyte to detect due to its widespread use in biological assays. Thus, chiral thin films were immersed in BSA aqueous solutions with concentrations ranging from 0 to 50 μM. The BSA detection was based on monitoring the wavelength shift of the CD signal at the crossing point (Figure 5D), which reflects changes in the local RI as a function of the BSA concentration. As the concentration of BSA increased, the CD spectra exhibited a gradual redshift till reaching a plateau. Unlike conventional protein detection methods that rely on far-UV CD associated with intrinsic protein optical activity, this approach leverages the plasmonic CD response of the substrate. These results demonstrate that C-AuNRs-based substrates are not only suitable for refractive index detection in highly absorbent media but also hold promise for label-free biosensing applications.

3. Conclusion

We have demonstrated a single-step seeded growth strategy for synthesizing colloidal chiral gold nanorods (C-AuNRs) with tunable optical activity in the visible range. By controlling

the molar ratio of achiral AuNR seeds to Au(III) ions and employing L- and D-cysteine as chiral inducers, we achieved efficient and rapid fabrication of C-AuNRs with rich chiroptical features. CD analysis revealed high RIS and a FoM exceeding 1000 RIU^{-1}, outperforming the conventional extinction-based sensing methods. We further demonstrated that thin films of C-AuNRs fabricated via layer-by-layer assembly retained their bisignate CD response and RIS performance, while exhibiting excellent stability, reusability, and resilience in highly absorbing media. These experimental findings were corroborated by simulations using electron tomography reconstructions as model input. Finally, as a proof of concept, we successfully applied the CD-based RIS response of C-AuNRs for the detection of BSA, highlighting their potential for sensitive biosensing. Overall, this work underscores the transformative potential of colloidal chiral plasmonic nanostructures for next-generation high-performance optical sensors and lays the foundation for exploring other chiral nanoparticle geometries in RI-based(bio)sensing.[6,45]

4. Experimental Section

Materials: Hexadecyltrimethylammonium Bromide (CTAB > 99.9%) was purchased from Acros Organics. $HAuCl_4{\cdot}3H_2O$, $NaBH_4$, ascorbic acid (AA), silver nitrate ($AgNO_3$), Hexadecyltrimethylammonium chloride (CTAC > 98%), *L-cysteine, D-cysteine*, sodium chloride (NaCl), poly-(diallyldimethylammonium chloride) (PDDA, 20 wt. % in H_2O, average M_w 200000–350000), poly-(sodium 4-styrenesulfonate) (PSS, M_w 70000), polyvinylpyrrolidone (PVP, average M_w 40000), H_2SO_4, hydrogen peroxide (H_2O_2, 28%) and glycerol were purchased to Sigma–Aldrich. Milli-Q grade water was used in all the syntheses.

Methods—Synthesis of AuNRs: AuNRs were synthesized following a previously published protocol with slight modifications.[46] Briefly, a gold NP seed was prepared by mixing 4.7 mL of 0.1 M CTAB with 25 µL of 50 mM $HAuCl_4$ and 400 µL of 10 mM $NaBH_4$ under vigorous stirring. After 1 min, the solution was kept at 27 °C for 1 h under gentle stirring. Then, 4 µL of the seeds were added to a growth solution containing 10 mL of 0.1 M CTAB, 100 mL of 50 mM $HAuCl_4$, 75 µL of 100 mM AA, and 100 µL of 10 mM $AgNO_3$. After keeping the reaction for 2 h at 27 °C, the AuNRs were washed twice by centrifugation and redispersed in 10 mM CTAC. The resulting AuNRs had an average length of 79 ± 6.7 nm and an average width of 32 ± 1.4 nm.

Methods—Synthesis of C-AuNRs: C-AuNRs were synthesized following a previously reported protocol.[3] A certain amount of the 5 mM AuNRs (containing 10 mM CTAC) was added as seed to a growth solution at 40 °C, containing 4 mL of 15 mM CTAC, 100 µL of 10 mM $HAuCl_4$, 475 µL of 100 mM AA, and 60 µL of 10 µM *L-cysteine* or *D-cysteine*. The amount of 5 mM AuNRs added was varied between 8.8 and 44 µL to tune the Au^{3+}/AuNR seeds molar ratio (*R*) from 20 to 4. After 1 h at 40 °C, the resulting dispersion was centrifuged and C-AuNRs redispersed in water to remove the excess reactants from the reaction flask.

Methods—Fabrication of Chiral Thin Films: The chiral thin films were obtained following the layer-by-layer method as previously reported.[47] First, glass slides were activated with piranha solution (H_2SO_4/ H_2O_2 3:1) for 30 min and then copiously rinsed with water and stored in water until use. Glass slides were cut to dimensions of ≈5 × 20 mm. The activated glass slides were immersed in Eppendorf tubes containing an aqueous solution of 1 mg mL^{-1} PDDA and 0.5 M NaCl for 15 min, rinsed with water, and then dried. The process was repeated using a negative polyelectrolyte aqueous solution containing 1 mg mL^{-1} PSS and 0.5 M NaCl, and then the PDDA solution. Note: PDDA and PSS solutions were sonicated for 10 min before use.

To deposit the C-AuNRs on a glass slide, first, it was necessary to perform A PVP functionalization to give them a negative charge. For that, the C-AuNRs solution was added dropwise to an aqueous solution containing 60 molecules of PVP per nm^2. After 3 h of stirring, the PVP-coated C-AuNRs were centrifuged twice and redispersed in ethanol. The final concentration of PVP-coated C-AuNRs was 1 mM. Then, the PDDA functionalized glass slide was immersed in the PVP-coated C-AuNR solution for 3 h under stirring and finally rinsed with water and dried with an air stream. The chiral thin films were kept in Eppendorf tubes until use.

Methods—Analysis of the Refractive Index Sensitivity of Colloidal C-AuNR: The refractive index sensitivity analysis was carried out by redispersing 100 µL of 5 mM C-AuNRs in 3 mL of glycerol/water mixtures with glycerol volume % of 0, 20, 40, 60, and 80, making the refractive index of the medium 1.33, 1.35, 1.37, 1.4, and 1.44, respectively. The samples were homogenized, and UV–vis and CD spectra were measured.

Methods—Analysis of Refractive Index Sensitivity of Chiral Thin Films: The chiral thin film was immersed in a 1 cm cuvette containing glycerol/water mixtures with glycerol volume % of 0, 20, 40, 60, and 80, making the refractive index of the medium 1.33, 1.35, 1.37, 1.4, and 1.44, respectively. After each immersion, the UV–vis and CD spectra were measured.

Methods—Refractive Index Sensitivity in Highly Absorbent Environments: A chiral thin film was immersed in a 1 cm cuvette containing glycerol/water mixtures with 10 µM CV (a concentration sufficient to saturate the extinction spectra, making it difficult to resolve the C-AuNPs optical features in the UV–vis) and varying glycerol volume percentages of 0, 20, 40, 60, and 80%, corresponding to refractive index of 1.33, 1.35, 1.37, 1.40, and 1.44, respectively. After each immersion, UV–vis and CD spectra were measured.

Methods—Analysis of Refractive Index Sensitivity of Chiral Thin Films for BSA Detection: To evaluate the sensitivity of the chiral thin film to changes in refractive index, the film was sequentially immersed in a 0.5 cm pathlength cuvette containing BSA solutions at concentrations ranging from 0 to 50 µM. After each exposure, both UV–vis–NIR and CD spectra were acquired to assess the optical response.

Methods—Simulations: Theoretical modeling often relies on the numerical simulation of Maxwell's equations to interpret experimental measurements of plasmon resonance modes. This is typically done using simplified models that closely resemble the experimental structure of interest.[48] Herein, we have employed electron tomography reconstructions as model input for detailed electromagnetic simulations utilizing the full-wave M3 Maxwell's solver.[49] The model used for the simulations consisted of a flat glass substrate with 3000 C-AuNRs randomly distributed on one side (Figure S11, Supporting Information), each NP identical and taken from the electron tomography reconstruction shown in Figure 2A. The simulated surface coverage was 17%, with an average interparticle distance of ≈3.25 nm. Considering the inherent complexity of developing a mechanistic colloidal deposition algorithm that accounts for the various attractive and repulsive forces required to produce a realistic CAD model of the deposition, we opted instead to construct a CAD model mimicking the SEM images in Figure 4A (Figure S11, Supporting Information). For the single-particle analysis shown in Figure S12 (Supporting Information), the CD spectrum was obtained for each particle orientation by performing rotations around both the longitudinal and transversal axes of the nanoparticle (NP). M3 full-wave Maxwell's solver is an efficient and highly accurate surface integral equation (SIE) solver based on the variational discretization of the method of moments.[35] In contrast to conventional volumetric formulations, the present method requires the parametrization solely of material boundaries and interfaces, thereby yielding a substantial reduction in the overall computational domain. The SIEs are discretized within a Galerkin framework, wherein divergence-conforming basis and testing functions are employed to variationally enforce the boundary conditions of the electromagnetic fields across the entire interface. Through this procedure, a high degree of accuracy is attained in the characterization of the resonant plasmonic response. Furthermore, the electromagnetic properties of gold are incorporated by adopting its frequency-dependent complex permittivity, as obtained from optical measurement data, ensuring a physically consistent representation of the dispersive material behavior.[50] To mitigate the prohibitive computational demand in solving large-scale assemblies, it incorporates spectral compression through the multilevel fast multipole algorithm combined with the fast Fourier transform (MLFMA-FFT).[51,52] This technique compresses the otherwise dense SIE-MoM

matrix, reducing both memory and time requirements. Additionally, the domain decomposition method (DDM)[53,54] is employed as a Schwarz preconditioner to expedite convergence and leverage particle pattern repetition, further minimizing computational costs. This methodology provides a highly efficient algorithm with scalable parallel performance on multicore computer clusters. The simulations were carried out on a workstation with two AMD EPYC 7H12 64-Core Processor 32 MB Smart-Cache processors at 2.60 GHz. A high surface mesh density was considered, leading to dense matrix systems of up to 17 million unknowns. A relative error norm of 10^{-6} was prescribed to stop the Krylov iterative solver. Considering the above, the computation times per wavelength were ≈2.5 h per sample, with a memory consumption up to 300 GB (a total of 130 h for each spectral analysis).

Supporting Information

Supporting Information is available from the Wiley Online Library or from the author.

Acknowledgements

Authors acknowledge the support from MICIU/AEI/10.13039/5011000 11033 and ERDF/EU (Grants: TED2021-131628A-I00, CNS2022-135531, PID2022-138724NB-I00, and PID2023-147567NB-I00), Consellería de Cultura, Educación e Ordenación Universitaria, Xunta de Galicia, and European Union Next Generation EU/PRTR (Grants: GPC ED431B 2025/42 and GRC ED431C 2020/09), EIC PATHFINDER Challenges (Grant: 101162112 (RADIANT)) and ERC SyG (Grant: 101166855 CHIRAL-PRO). Funding for open access was provided by Universidade de Vigo/CISUG

Conflict of Interest

The authors declare no conflict of interest.

Data Availability Statement

The data that support the findings of this study are available from the corresponding author upon reasonable request.

Keywords

biosensing, chiral colloidal nanocrystals, chiral gold nanorods, circular dichroism, refractive index sensing, seed-mediated growth

Received: August 6, 2025
Revised: October 1, 2025
Published online:

[1] Y. Yao, O. Ávalos-Ovando, T. Ding, R. A. Alvarez-Puebla, P. Yu, E. Ashalley, L. Ma, Z. Wang, G. Markovich, A. O. Govorov, *Chem* **2025**, *11*, 102544.
[2] L. Tan, W. Fu, Q. Gao, P.-P. Wang, *Adv. Mater.* **2024**, *36*, 2309033.
[3] B. Ni, M. Mychinko, S. Gómez-Graña, J. Morales-Vidal, M. Obelleiro-Liz, W. Heyvaert, D. Vila-Liarte, X. Zhuo, W. Albrecht, G. Zheng, G. González-Rubio, J. M. Taboada, F. Obelleiro, N. López, J. Pérez-Juste, I. Pastoriza-Santos, H. Cölfen, S. Bals, L. M. Liz-Marzán, *Adv. Mater.* **2023**, *35*, 2208299.
[4] A. Ben-Moshe, A. O. Govorov, G. Markovich, *Angew. Chem. Inter. Ed.* **2013**, *52*, 1275.
[5] W. Liu, Z. Zhu, K. Deng, Z. Li, Y. Zhou, H. Qiu, Y. Gao, S. Che, Z. Tang, *J. Am. Chem. Soc.* **2013**, *135*, 9659.
[6] K. Kant, R. Beeram, Y. Cao, P. S. S. dos Santos, L. González-Cabaleiro, D. García-Lojo, H. Guo, Y. Joung, S. Kothadiya, M. Lafuente, Y. X. Leong, Y. Liu, Y. Liu, S. S. B. Moram, S. Mahasivam, S. Maniappan, D. Quesada-González, D. Raj, P. Weerathunge, X. Xia, Q. Yu, S. Abalde-Cela, R. A. Alvarez-Puebla, R. Bardhan, V. Bansal, J. Choo, L. C. C. Coelho, J. M. M. M. de Almeida, S. Gómez-Graña, M. Grzelczak, et al., *Nanoscale Horiz.* **2024**, *9*, 2085.
[7] G. Zheng, J. He, V. Kumar, S. Wang, I. Pastoriza-Santos, J. Pérez-Juste, L. M. Liz-Marzán, K.-Y. Wong, *Chem. Soc. Rev.* **2021**, *50*, 3738.
[8] A. Guerrero-Martínez, M. Grzelczak, L. M. Liz-Marzán, *ACS Nano* **2012**, *6*, 3655.
[9] N. Fiuza-Maneiro, J. Mendoza-Carreño, S. Gómez-Graña, M. I. Alonso, L. Polavarapu, A. Mihi, *Adv. Mater.* **2024**, *36*, 2413967.
[10] J. Mendoza-Carreño, P. Molet, C. Otero-Martínez, M. I. Alonso, L. Polavarapu, A. Mihi, *Adv. Mater.* **2023**, *35*, 2210477.
[11] P. Lodahl, S. Mahmoodian, S. Stobbe, A. Rauschenbeutel, P. Schneeweiss, J. Volz, H. Pichler, P. Zoller, *Nature* **2017**, *541*, 473.
[12] Y. Negrín-Montecelo, A. Movsesyan, J. Gao, S. Burger, Z. M. Wang, S. Nlate, E. Pouget, R. Oda, M. Comesaña-Hermo, A. O. Govorov, M. A. Correa-Duarte, *J. Am. Chem. Soc.* **2022**, *144*, 1663.
[13] Y.-Y. Lee, R. M. Kim, S. W. Im, M. Balamurugan, K. T. Nam, *Nanoscale* **2019**, *12*, 58.
[14] S. Gómez-Graña, J. Pérez-Juste, R. A. Alvarez-Puebla, A. Guerrero-Martínez, L. M. Liz-Marzán, *Adv. Opt. Mater.* **2013**, *1*, 477.
[15] J. L. Paris, G. Villaverde, S. Gómez-Graña, M. Vallet-Regí, *Acta Biomater.* **2020**, *101*, 459.
[16] C. Hamon, L. M. Liz-Marzán, *J. Colloid Inter. Sci.* **2018**, *512*, 834.
[17] L. Zhang, Y. Chen, J. Zheng, G. R. Lewis, X. Xia, E. Ringe, W. Zhang, J. Wang, *Angew. Chem. Inter. Ed.* **2023**, *62*, 202312615.
[18] A. Guerrero-Martínez, B. Auguié, J. L. Alonso-Gómez, Z. Džolić, S. Gómez-Graña, M. Žinić, M. M. Cid, L. M. Liz-Marzán, *Angew. Chem. Inter. Ed.* **2011**, *50*, 5499.
[19] G. González-Rubio, J. Mosquera, V. Kumar, A. Pedrazo-Tardajos, P. Llombart, D. M. Solís, I. Lobato, E. G. Noya, A. Guerrero-Martínez, J. M. Taboada, F. Obelleiro, L. G. MacDowell, S. Bals, L. M. Liz-Marzán, *Science* **2020**, *368*, 1472.
[20] M. Obelleiro-Liz, V. F. Martín, D. M. Solís, J. M. Taboada, F. Obelleiro, L. M. Liz-Marzán, *Adv. Opt. Mater.* **2023**, *11*, 2203090.
[21] X. Pan, H. Li, X. Chen, S. Wang, S. Mourdikoudis, T. Luo, K. Wong, G. Zheng, *Adv. Opt. Mater.* **2025**, 2403422.
[22] S. W. Im, R. M. Kim, J. H. Han, I. H. Ha, H.-E. Lee, H.-Y. Ahn, E. Jo, K. T. Nam, *Nat. Protoc.* **2025**, *20*, 1082.
[23] N.-N. Zhang, Z.-L. Shen, S.-Y. Gao, F. Peng, Z.-J. Cao, Y. Wang, Z. Wang, W. Zhang, Y. Yang, K. Liu, T. Sun, *Adv. Opt. Mater.* **2023**, *11*, 2203119.
[24] N.-N. Zhang, M. Mychinko, S.-Y. Gao, L. Yu, Z.-L. Shen, L. Wang, F. Peng, Z. Wei, Z. Wang, W. Zhang, S. Zhu, Y. Yang, T. Sun, L. M. Liz-Marzán, S. Bals, K. Liu, *Nano Lett.* **2024**, *24*, 13027.
[25] G. Klös, M. Miola, D. S. Sutherland, *J. Phys. Chem. C* **2019**, *123*, 7347.
[26] Y. Xu, P. Bai, X. Zhou, Y. Akimov, C. E. Png, L.-K. Ang, W. Knoll, L. Wu, *Adv. Opt. Mater.* **2019**, *7*, 1801433.
[27] B. Tadgell, L. M. Liz-Marzán, *Chem. - Eur. J.* **2023**, *29*, 202301691.
[28] J. Kumar, H. Eraña, E. López-Martínez, N. Claes, V. F. Martín, D. M. Solís, S. Bals, A. L. Cortajarena, J. Castilla, L. M. Liz-Marzán, *Proc. Natl. Acad. Sci. USA* **2018**, *115*, 3225.
[29] S. Rodal-Cedeira, V. Montes-García, L. Polavarapu, D. M. Solís, H. Heidari, A. La Porta, M. Angiola, A. Martucci, J. M. Taboada, F. Obelleiro, S. Bals, J. Pérez-Juste, I. Pastoriza-Santos, *Chem. Mat.* **2016**, *28*, 9169.
[30] H.-H. Jeong, A. G. Mark, M. Alarcón-Correa, I. Kim, P. Oswald, T.-C. Lee, P. Fischer, *Nat. Commun.* **2016**, *7*, 11331.

[31] P. Chen, N. T. Tran, X. Wen, Q. Xiong, B. Liedberg, *ACS Sens.* **2017**, *2*, 235.
[32] L. Scarabelli, A. Sánchez-Iglesias, J. Pérez-Juste, L. M. Liz-Marzán, *J. Phys. Chem. Lett.* **2015**, *6*, 4270.
[33] H.-E. Lee, H.-Y. Ahn, J. Mun, Y. Y. Lee, M. Kim, N. H. Cho, K. Chang, W. S. Kim, J. Rho, K. T Nam, *Nature* **2018**, *556*, 360.
[34] B. Ni, G. González-Rubio, F. Kirner, S. Zhang, H. Cölfen, *Angew. Chem. Inter. Ed* **2022**, *61*, 202200753.
[35] D. M. Solís, J. M. Taboada, F. O. Basteiro, *IEEE Trans. Antennas Propag.* **2015**, *63*, 2141.
[36] B. Sepúlveda, P. C. Angelomé, L. M. Lechuga, L. M. Liz-Marzán, *Nano Today* **2009**, *4*, 244.
[37] R. Mehra, *Chem. Sci. J.* **2003**, *115*, 147.
[38] V. K. Valev, J. J. Baumberg, C. Sibilia, T. Verbiest, *Adv. Mater.* **2013**, *25*, 2517.
[39] M. A. Otte, B. Sepúlveda, W. Ni, J. P. Juste, L. M. Liz-Marzán, L. M. Lechuga, *ACS Nano* **2010**, *4*, 349.
[40] N. Maccaferri, K. E. Gregorczyk, T. V. A. G. de Oliveira, M. Kataja, S. van Dijken, Z. Pirzadeh, A. Dmitriev, J. Åkerman, M. Knez, P. Vavassori, *Nat. Commun.* **2015**, *6*, 6150.
[41] A. U. Khan, S. Zhao, G. Liu, *J. Mater. Chem. C* **2016**, *120*, 19353.
[42] K. Claborn, C. Isborn, W. Kaminsky, B. Kahr, *Angew. Chem. Inter. Ed.* **2008**, *47*, 5706.
[43] N. A. Kotov, L. M. Liz-Marzán, P. S. Weiss, *ACS Nano* **2021**, *15*, 12457.
[44] J.-Y. Kim, C. McGlothin, M. Cha, Z. J. Pfaffenberger, E. S. Turali Emre, W. Choi, S. Kim, J. S. Biteen, N. A. Kotov, *Adv. Sci.* **2024**, *121*, 2312082121.
[45] L. Polavarapu, J. Pérez-Juste, Q.-H. Xu, L. M. Liz-Marzán, *J. Mater. Chem. C* **2014**, *2*, 7460.
[46] S. Gómez-Graña, F. Hubert, F. Testard, A. Guerrero-Martínez, I. Grillo, L. M. Liz-Marzán, O. Spalla, *Langmuir* **2011**, *28*, 1453.
[47] S. Vial, I. Pastoriza-Santos, J. Pérez-Juste, L. M. Liz-Marzán, *Langmuir* **2007**, *23*, 4606.
[48] V. Myroshnychenko, J. Rodríguez-Fernández, I. Pastoriza-Santos, A. M. Funston, C. Novo, P. Mulvaney, L. M. Liz-Marzán, F. J. García de Abajo, *Chem. Soc. Rev.* **2008**, *37*, 1792.
[49] D. M. Solís, J. M. Taboada, F. Obelleiro, L. M. Liz-Marzán, F. J. García de Abajo, *ACS Nano* **2014**, *8*, 7559.
[50] P. B. Johnson, R. W. Christy, *Phys. Rev. B* **1972**, *6*, 4370.
[51] D. M. Solís, J. M. Taboada, F. Obelleiro, L. M. Liz-Marzán, F. J. García de Abajo, *ACS Photonics* **2017**, *4*, 329.
[52] J. M. Taboada, M. G. Araujo, F. Obelleiro, J. L. Rodríguez, L. Landesa, *Proc. IEEE, Spec. Issue Large Scale Electromagn. Comput. Model., Appl.* **2013**, *101*, 350.
[53] V. F. Martín, D. Larios, D. M. Solís, J. M. Taboada, L. Landesa, F. Obelleiro, *IEEE Access* **2020**, *8*, 107345.
[54] D. M. Solís, F. Obelleiro, J. M. Taboada, *IEEE Photonics J.* **2016**, *8*, 14